




# A detailed investigation on the structural, optical, and photocatalytic properties of ZnO@ZnS core–shell nanostructures

A. Suguna<sup>1</sup>, S. Prabhu<sup>2</sup>, R. Siranjeevi<sup>2</sup>, S. Pugazhendhi<sup>2</sup>, and C. Sridevi<sup>3,\*</sup> 

<sup>1</sup>Department of Physics, Shri Sakthikailash Women's College, Salem, Tamilnadu 636 003, India

<sup>2</sup>Department of Physics, Saveetha School of Engineering, Saveetha Institute of Medical and Technical Sciences (SIMATS), Thandalam, Chennai, Tamil Nadu 602 105, India

<sup>3</sup>Department of Physics, Sri Sarada College for Women, Salem, Tamilnadu 636 016, India

Received: 2 June 2023

Accepted: 25 July 2023

Published online:

11 August 2023

© The Author(s), under exclusive licence to Springer Science+Business Media, LLC, part of Springer Nature 2023

## ABSTRACT

In this study, zinc oxide nanoparticles were synthesized via a facile hydrothermal and solvothermal method and were covered by zinc sulfate using a chemical approach forming ZnO@ZnS core–shell nanostructures. Different techniques like XRD, BET, FESEM, PL, and UV–Vis spectroscopy as well as photocatalytic activity of ZnO, ZnS, and ZnO@ZnS results were investigated to confirm the nanostructure and homogeneous distribution of particles inside the matrix. In addition, the scavenger study indicates that all charge carriers and reactive radicals contribute by roughly close extent, which explains the observed increase in the rate of degradation. The photocatalytic activity was evaluated under UV light toward MO and RhB dyes. For degrading MO solution under UV irradiation, it is found that both the photocatalytic performances of ZnO@ZnS are much higher (98.6%) than those of pure ZnO (54%). The photocatalytic mechanism under UV light irradiation was proposed. The complex ZnO@ZnS nanocable provide a facile, low cost, high surface-to-volume ratio, high photocatalytic efficiency, and high reusability, which shall be also promising in many related areas, such as solar energy conversion, water splitting, and energy storage.

## 1 Introduction

Water is a fundamental requirement of life. The availability of fresh water is crucial for life-sustaining activities, like drinking, cooking, cleaning, and

agriculture. Modern human activity has however polluted the water a lot. Toxic chemicals and harmful microorganisms are present in most natural drinking water supplies. According to the World Health Organization, there are around 4 billion instances of

Address correspondence to E-mail: sriphysics1@gmail.com

water-related disorders recorded each year [1]. Water contamination from leftover colors from many industries is a big problem nowadays. Many different organic contaminants have been transported into natural water resources [2–5] due to human activities, such as the textile, paper, plum, dye, pharmaceutical, sunburn, craft, and whitening sectors. Since these contaminants are poisonous to living things, they must be eliminated before being released into the environment. The study of disinfectant processes is now vital to the survival of the human species. Physical and chemical methods, such as chlorination, coronation, and UV treatment, are presently used to cleanse water [6, 7]. Recently, it has come to light that nanotechnology may be used in the extraction of minute contaminants from wastewater [8–11]. In compared to more traditional methods, heterogeneous photocatalysis is presently being regarded a potential strategy for water purification. Toxic chemical compounds with long chains may be cleaved into smaller, less dangerous pieces. Photocatalysts with a nanostructure have a high surface-to-volume ratio, which means they can absorb more of the molecules of interest. It provided a viable strategy for eliminating dye pollution in water treatment facilities [12].

In recent years, not only has ZnO benefited from impurity loading but also from surface enhancement, allowing for the development of several unique characteristics [13]. ZnO plus a different semiconductor may generate a heterostructure that exhibits a powerful photoelectric effect in solar cells [14, 15]. Many researchers are interested in using ZnS with a broad band gap as a photocatalyst, photoconductor, optical detector, or electroluminescent substance [16]. The band gap of ZnS (3.51 eV) is very close to ZnO (3.45 eV), and theoretical calculations and experimental results have demonstrated that the combination of these two semiconductors could yield a novel composite with the photoexcitation threshold energy lower than those of the individual components [17]. Nanoring, biaxial nanowire, and saw-like nanostructure ZnO/ZnS core/shell composites have all been described so far. Moreover, the ZnS/ZnO core-shell structures have been favorable for increasing the photocatalytic property for example, For example, Chin-Chi Cheng et al. [18] fabricated ZnO/ZnS core-shell nanostructure by facile hydrothermal method for optoelectronic applications. Taher Ghrif et al. synthesize ZnO/ZnS core-shell nanowires by

electrodeposition method for catalytic applications [19]. In this paper, a novel spherical ZnO/ZnS core/shell particle structure was obtained after sulfurizing ZnO spheres by a Na<sub>2</sub>S solution under the hydrothermal condition. The pure spherical ZnO particles were firstly synthesized via a simple mild solvothermal approach by the assistance of diethylene glycol. Then, the partial ZnO molecules on the surface of the ZnO spheres were converted to ZnS molecules with the presence of S<sup>2-</sup> ions under the hydrothermal condition and finally a ZnS shell structure was formed over the surface of ZnO spheres. More importantly, the hydrothermal route is one of the best and well-known synthesis methods of nanoparticles. This method is highly efficient and economical and particle size can be controlled easily by varying experimental conditions like (temperature, pressure, and time). The prepared samples were then characterized using XRD, SEM, EDX, DRS, and PL to investigate their improved structural, optical, and morphological properties. The photocatalytic activity of the ZnO/ZnS core/shell composite was evaluated by monitoring MO and RhB degradation as the probe reaction. The results demonstrate that ZnO@ZnS core-shell nanoparticles showed outstanding degradation, higher kinetic rate, and long-term stability. The improved photocatalytic mechanism was also discussed. Moreover, the complex ZnO/ZnS core-shell nanoparticles provide a facile, low cost, high surface-to-volume ratio, high photocatalytic efficiency, and high reusability, which shall be also promising in many related areas, such as solar energy conversion, water splitting, and energy storage.

## 2 Experimental section

### 2.1 Preparation of ZnO spheres

The synthesis procedure is as follows: Zn(CH<sub>3</sub>COO)<sub>2</sub>·2H<sub>2</sub>O (3 mmol) was submerged in DEG (10 mL) at 85 °C for 2 h while being vigorously stirred. The pH of the solution was found to be 6.5, which is measured using digital pH meter. After being mixed, the aforesaid ingredients were placed into a Teflon-lined autoclave, heated to 100 °C for 12 h, and then allowed to cool to ambient temperature. After that, the ethanol and distilled water were used to wash and filter the residue. Pure spherical

ZnO particles were produced after drying the precipitate under vacuum at 60 °C for 3 h.

## 2.2 Synthesis of ZnO/ZnS core/shell particles

The obtained spherical ZnO sample as the template was added into a Na<sub>2</sub>S solution and then vigorously stirred for 20 min. The mixed solution was placed in an autoclave coated with Teflon and heated to 160 °C for 8 h. Centrifugation is then used to separate the results (ZnO/ZnS core/shell precipitates), which were subsequently rinsed in ethanol and deionized water before being dried at 60 °C under vacuum for 3 h.

## 2.3 Characterization techniques

To identify the crystal structure, X-ray diffraction studies were carried out using PANalytical X-ray diffractometer with nickel-filtered CuK $\alpha$  (30 kV, 30 mA). The surface morphology of the samples was studied using scanning electron microscopy (SEM; S-4100, Hitachi). The Fourier transform infrared spectroscopy (FTIR) of the materials was carried out using Fourier transform infrared spectrometer (FTIR, Nexus 670). The X-ray photoelectron spectroscopy spectra (XPS) of ZnO/ZnS core/shell particles were recorded via Thermo ESCALAB 250 at room temperature. Photoadsorption spectra of catalysts were tested by UV–Vis diffuse reflectance spectroscopy (DRS Hitachi UV-3600). Photoluminescence spectra (PL) of CdS-DETA-based samples were tested with FLS920 fluorescence lifetime and steady-state spectrometer. Specific surface area values (SBET) were tested with ASAP2020 instrument. X-ray photoelectron spectroscopy (XPS) analyses were obtained on X-ray Photoelectron Spectrometer (ESCALAB 250XI).

## 2.4 Photocatalytic set-up

The degradation of methylene blue (MB) and rhodamine B (RhB) solutions was used to evaluate the photocatalytic activity of complex ZnO/ZnS. For the photocatalytic activity evaluation, the concentration of photodegraded dye solution was recorded by a Hitachi U-2900 UV–Vis spectroscopy. Photocatalytic experiments were carried out in aqueous solution of MO and RhB employing a UVA emitting lamp (365 nm, Spectroline ENF-260) at dyes natural pH. A

5-mL portion of  $1 \times 10^{-5}$  M MO was placed in a quartz cell containing glass material (2 pieces, approximately 1 cm  $\times$  1 cm). Special attention was paid for contacting the dye solution and UV light with glass surface and solutions were shaken continuously. The absorption of MB at 664 nm (UV–Vis Dr. Lange CADAS 200 Spectrometer) was monitored over 60 min in the presence and absence of light or glass material. At regular intervals of irradiation, aliquots of 2 mL were sampled and then absorption was measured in terms of change in intensity at 664 nm. The decolorization and photocatalytic degradation efficiency have been calculated as Efficiency ( $\eta$ ) =  $(C - C_0)/C \times 100$ , where  $C_0$  and  $C$  correspond to the initial and final concentration of dye before and after photo-irradiation. The schematic representation of the photocatalytic set-up is shown in Fig. 1a.

## 3 Results and discussion

### 3.1 XRD analysis

The XRD patterns of the pure ZnO NPs and the ZnO@ZnS are shown in Fig. 1b. For the ZnO NPs, the peaks can be indexed to the known hexagonal wurtzite structure of ZnO with lattice constants of  $a = b = 3.250 \text{ \AA}$  and  $c = 5.207 \text{ \AA}$  (JCPDF: 36–1451) and the sample is quite pure and no peaks of other ZnO phases were observed. It is possible that the ZnO NPs in ZnO@ZnS have been coated with a different substance, since the amplitude of the ZnO NPs' peaks is lower than that of pure ZnO NPs. In addition, the ZnS (JCPDF: 50–566) broad peak at  $29.12^\circ$  may be indicative of ZnS coatings on ZnO NPs. In addition, the diffraction peak of the ZnS (111) plane is much higher intense, suggesting that the ZnS nanoparticles created using the hydrothermal process are high crystalline nature. The average crystalline size is calculated from Debye–Scherrer's formula:

$$d = \frac{K\lambda}{\beta \cos \theta},$$

where  $d$  is the mean crystallite size,  $K$  is the shape factor taken as 0.89,  $\lambda$  is the wavelength of the incident beam,  $\beta$  is the full-width at half-maximum and  $\theta$  is the Bragg angle. The average crystalline size was found as 19 nm, 26 nm, and 33 nm for pure ZnO,

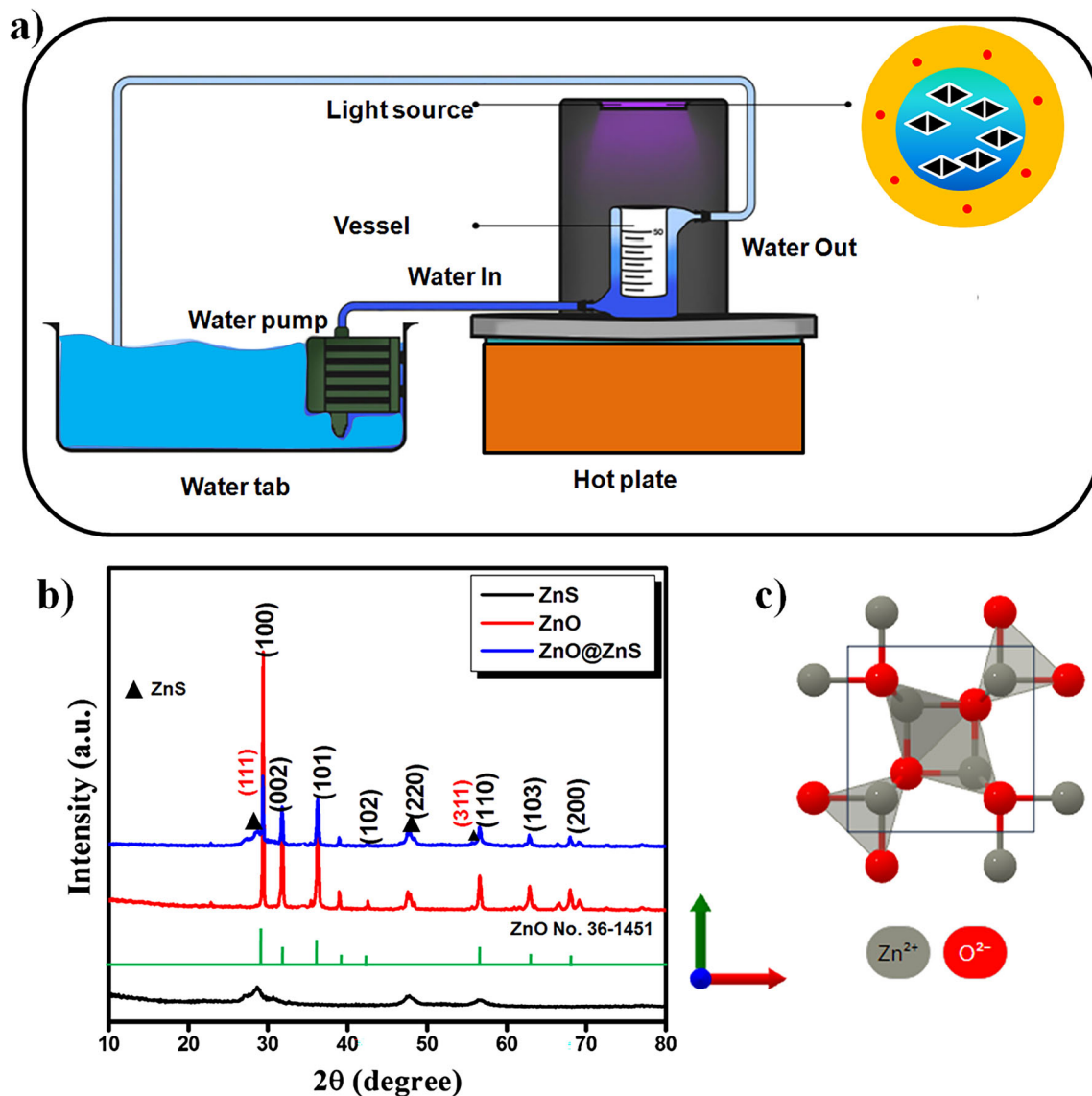


**Fig. 1** a Schematic representation of the photocatalytic set-up; b powder XRD pattern; and c crystal structure of ZnO

ZnS, and ZnO/ZnS composites, respectively. Figure 1c also shows the ZnO crystal structure.

### 3.2 Morphological analysis

The spherical ZnO and ZnO/ZnS core/shell particles produced are illustrated in Fig. 2 using SEM and TEM pictures. It is thought that the smooth and flawless spherical shape of pure ZnO particles played a crucial role in the creation of ZnO spheres using the solvothermal method (Fig. 2a). Nonetheless, as can be seen from the SEM image of the ZnO/ZnS core/shell framework shown in Fig. 2b, the rough exterior of the sample indicates that some of the ZnO

molecules on the surface of the ZnO spheres have been converted to ZnS particles in the presence of  $S_2^-$  ions under hydrothermal condition, ultimately forming ZnS shell structure. The TEM picture (Fig. 2c) also shows the core-shell nanoparticles in clear. In addition, as can be seen in Fig. 2d, ZnO NPs are really coated with ZnS, as shown by the HRTEM picture of the ZnO/ZnS. Furthermore, the comparable SAED pattern shows that the material is single crystallized and contains brilliant spots (Fig. 2e). The elemental mapping picture (Fig. 2f) also revealed the core-shell structure of ZnO/ZnS. Both ZnO and ZnS have the same atomic concentration of Zn. Therefore,



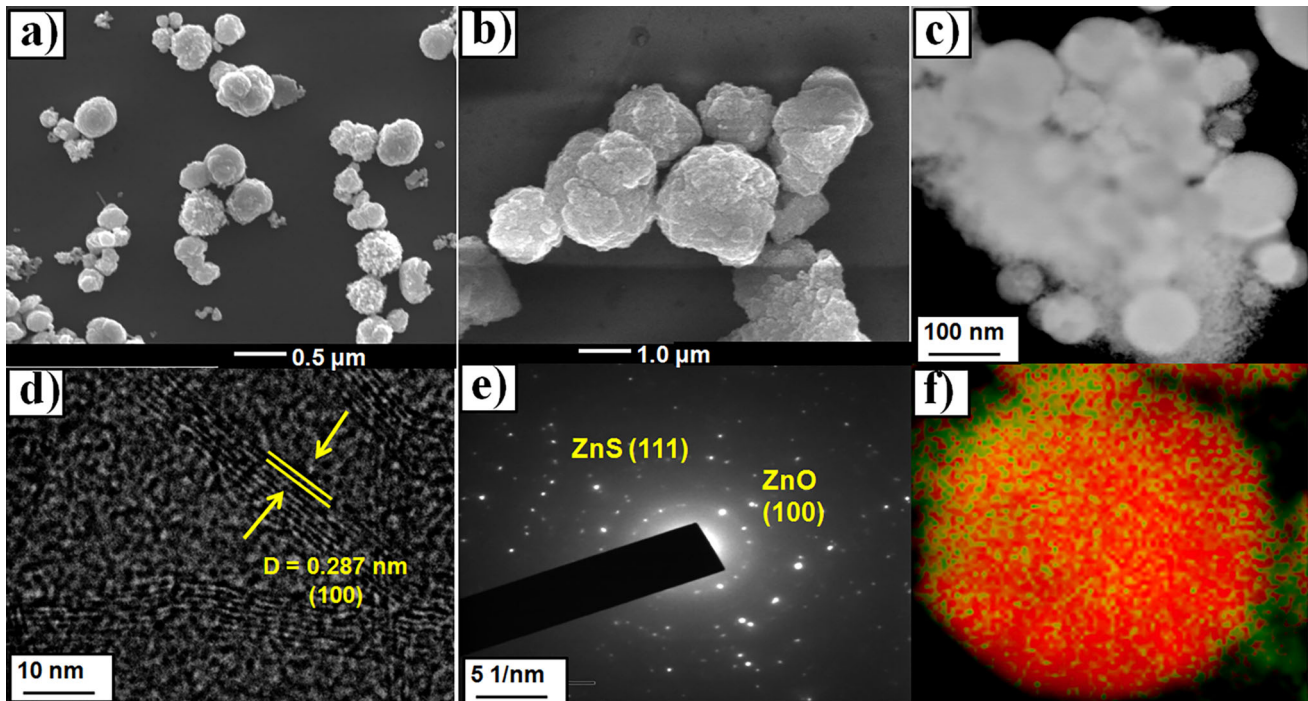


**Fig. 2** SEM images of **a** ZnO and **b** ZnO/ZnS; TEM image of **c** ZnO/ZnS; **d** HRTEM image of ZnO/ZnS; **e** SAED pattern of ZnO/ZnS; **f** elemental mapping of ZnO/ZnS

the distribution of sulfur and oxygen is crucial to tell ZnO apart from ZnS.

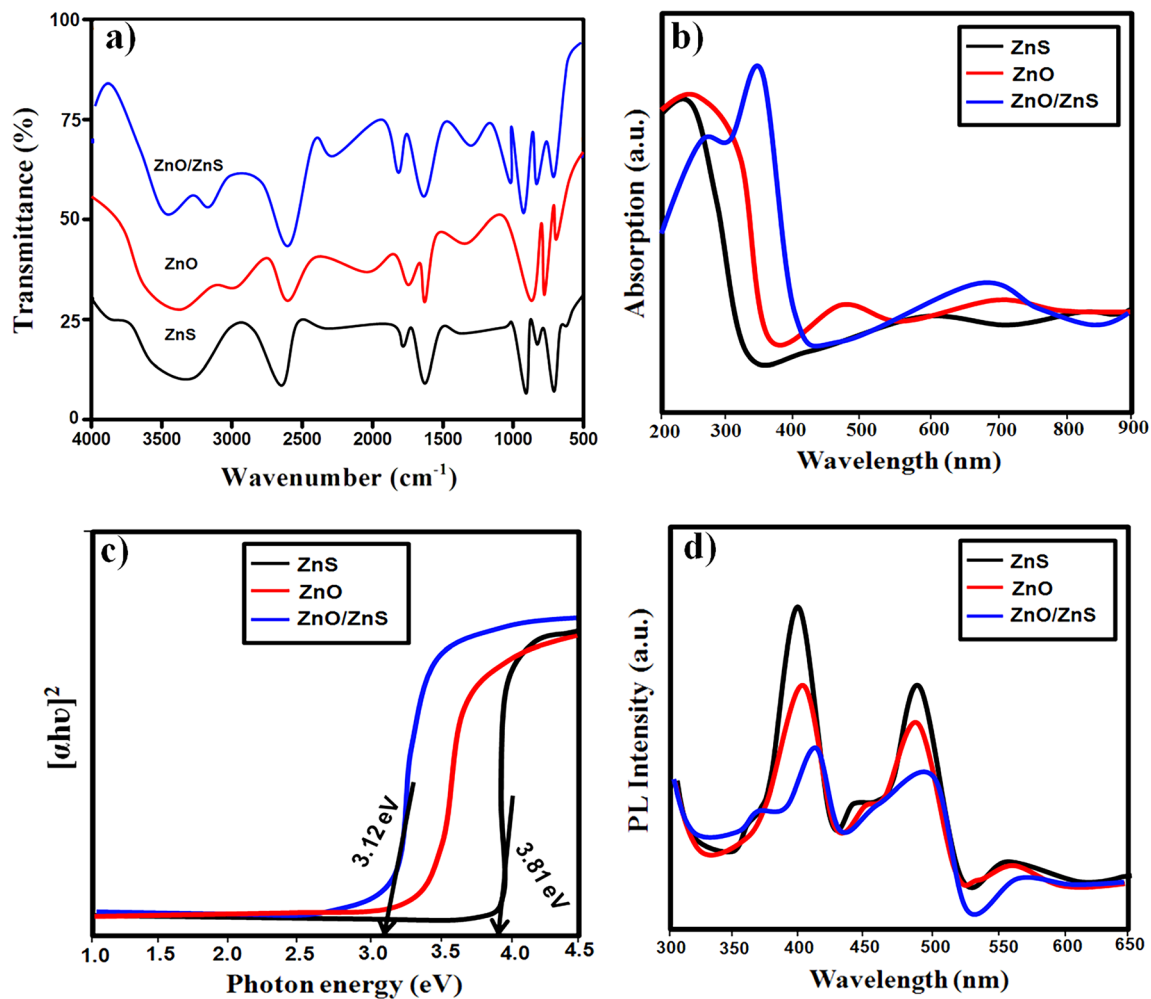
### 3.3 FTIR spectra analysis

Figure 3a displays the FTIR spectra obtained from ZnO, ZnS, and ZnO/ZnS composite materials. The unique vibration of ZnO [20] is explained by the fingerprint area peaks about 500 and 650  $\text{cm}^{-1}$  shown in Fig. 3a (except for ZnS). The stretching vibration of ZnS is represented by the peaks shown in Fig. 1 between 560 and 690  $\text{cm}^{-1}$  (with the exception of the ZnO peak). The peaks for ZnO and ZnS can be seen coexisting in the FTIR spectra of the composite samples (Fig. 3a). This finding allows us to verify that hetero-structured ZnO and ZnS are really formed in the synthesized ZnO/ZnS nanoparticles [21]. The hydroxyl (OH) group vibration is responsible for the peak at 2800–3400  $\text{cm}^{-1}$ , whereas the peaks between 1500–1650  $\text{cm}^{-1}$  and at 2370  $\text{cm}^{-1}$  are due to C = O [22].

### 3.4 Optical studies

In order to determine the wavelength spectrum of the chosen materials, it is crucial to measure the band

gap energy. In Fig. 3b, one can see the absorbance spectra of ZnS, ZnO, and ZnO/ZnS. The acquired findings show that light excitation across the energy spectrum accounts for the red shift to longer wavelengths seen at the band edge, from about 200–300 nm for ZnO to around 400–500 nm for ZnO/ZnS. From these spectra optical band gap energy ( $E_g$ ) was calculated using Kubelka–Munk equation, which is described by  $F(R_\infty) = K/S = (1 - R_\infty)^2/2R_\infty$ , where  $R_\infty = R_{\text{sample}}/R_{\text{standard}}$  is the reflectance of an infinitely thick specimen, while  $K$  and  $S$  are the absorption and scattering coefficients, respectively.  $F(R_\infty) \cdot (hv)^2 = A(hv - E_g)$ . The variation of  $F(R_\infty) \cdot (hv)^2$  versus  $hv$  was plotted and the straight line range of these plots is extended on the  $x$ -axis ( $hv$ ) to obtain the values of optical band gap ( $E_g$ ). Band gap energies of all the samples were estimated using the plot of  $F(R_\infty) \cdot (hv)^2$  versus photon energy ( $hv$ ) (Kubelka–Munk equation). In addition, as shown in Fig. 3c, the band gap energy ( $E_g$ ) is determined to be 3.81 eV for pure ZnS, 3.43 eV for ZnO, and 3.12 eV for ZnO/ZnS using the Tauc diagram [23]. On the contrary together, a large electron–hole spacing lengthens the duration of photocatalytic processes used to oxidize organic dyes [24]. When the light fall on the semi-conductors materials the charge separation occurred



**Fig. 3** **a** FTIR spectra of photocatalyst samples; **b** UV–Vis absorption spectra; **c** band gap plot; **d** room-temperature PL spectra of all the photocatalysts with excitation wavelength of 290 nm

and the recombination between the charge carriers induced photoluminescence signals and photoluminescence (PL) spectrum of the pure ZnO spheres, ZnS spheres, and ZnO/ZnS core/shell samples in ethanol suspension by excitation at 290 nm. Pure ZnO spheres have two faint PL peaks at 379 nm and 484 nm, as seen in Fig. 3d. The PL spectra of ZnO/ZnS core/shell material, nevertheless show a diminished PL peak at 364 nm and a faint peak at the original location of ZnO after interacting with Na<sub>2</sub>S. One of the PL peaks of ZnO/ZnS is redshifted from its pure ZnO counterpart and its intensity is much lower and more diffuse than that of pure ZnO. The strong association between zinc sulfide and zinc oxide nanoparticles was further confirmed by the fact that the presence of ZnO nanoparticles over ZnS in the (ZnO/ZnS) nanocomposites sample inhibited the

photoluminescence of ZnO peaks). Moreover, the decrease in PL emission intensity denoted the suppression of the recombination process of electron–hole pair. In our case, the emission intensity was significantly decreased for ZnO/ZnS core/shell sample. This could be due to the effective suppression of electron–hole recombination process and it can have positive influence in the improvement of charge transfer process and improve the photocatalytic activity.

### 3.5 Surface area and elemental composition analysis

ZnO and ZnO/ZnS pore size and N<sub>2</sub> adsorption–desorption data were obtained. Features of a mesoporous structure were reflected in the isotherm, which had a type IV curve [25–27]. Figure 4a shows

that the BET specific surface area of ZnO was  $97.6 \text{ m}^2\text{g}^{-1}$ , whereas that of ZnO/ZnS was  $116.9 \text{ m}^2\text{g}^{-1}$ . The results showed a positive correlation between the additional sulfur source and the particular surface area. Thus, the amount of ZnS particles determined how large the specific surface area would be. The obtained pore size (Fig. 4b) for ZnO was 32.4 nm, whereas for ZnO/ZnS, it was 44.5 nm. The photocatalyst can break down the dye solution in the presence of UV light because of its large specific area of surface, which allows for additional surface reaction sites. The high specific surface area increases the contact between the reactant solution and the photocatalyst, which provides more surface reaction sites to degrade the dye solution under UV light. Moreover, the porous structure thus reduce the local ZnO aggregate, which can significantly improve catalytic efficiency. XPS analysis was used to determine the surface elemental composition and binding energy state of the produced ZnO/ZnS. The presence of Zn, O, and S elements in the ZnO/ZnS sample is confirmed by a full-survey scan the spectrum, as shown in Fig. 4c. Zn  $2p_{3/2}$  and Zn  $2p_{1/2}$  were attributed to the two largest peaks in the Zn spectra (Fig. 4d) at 1021.6 and 1044.5 eV, respectively [28]. Figure 4e shows that the binding energy of S  $2p$

may be measured to be 163.2 eV. The Zn–S bond was found to have a binding energy of 163.2 eV [29]. Possibly as a result of chemisorbed oxygen (Och) in the ZnO sample, the O spectra in Fig. 4f were captured at 533.4 eV.

### 3.6 Photocatalytic studies

Photodegradation of MB and RhB in an aqueous solution under 10-W exposure to ultraviolet (UV) is used to compare the photocatalytic capabilities of ZnO and ZnO/ZnS core–shell nanocomposite photocatalyst. Absorption spectra (Fig. 5a–d) for MB and RhB solutions in ZnO and ZnO/ZnS photocatalysts. To track the catalytic decomposition process, we decided to use the MB (664 nm) and RhB (554 nm) distinctive absorption peaks. Since the exposure duration is increasing, the absorption peaks are becoming progressively weaker. This finding suggests that UV light irradiation in the presence of ZnO/ZnS leads to the progressive degradation of MB and RhB. Absorption spectra show that ZnO/ZnS photocatalysts are more effective than ZnO in degrading MB, suggesting that these materials have a greater photocatalytic activity. Over a ZnO/ZnS system, the rate at which MB and RhB degraded over

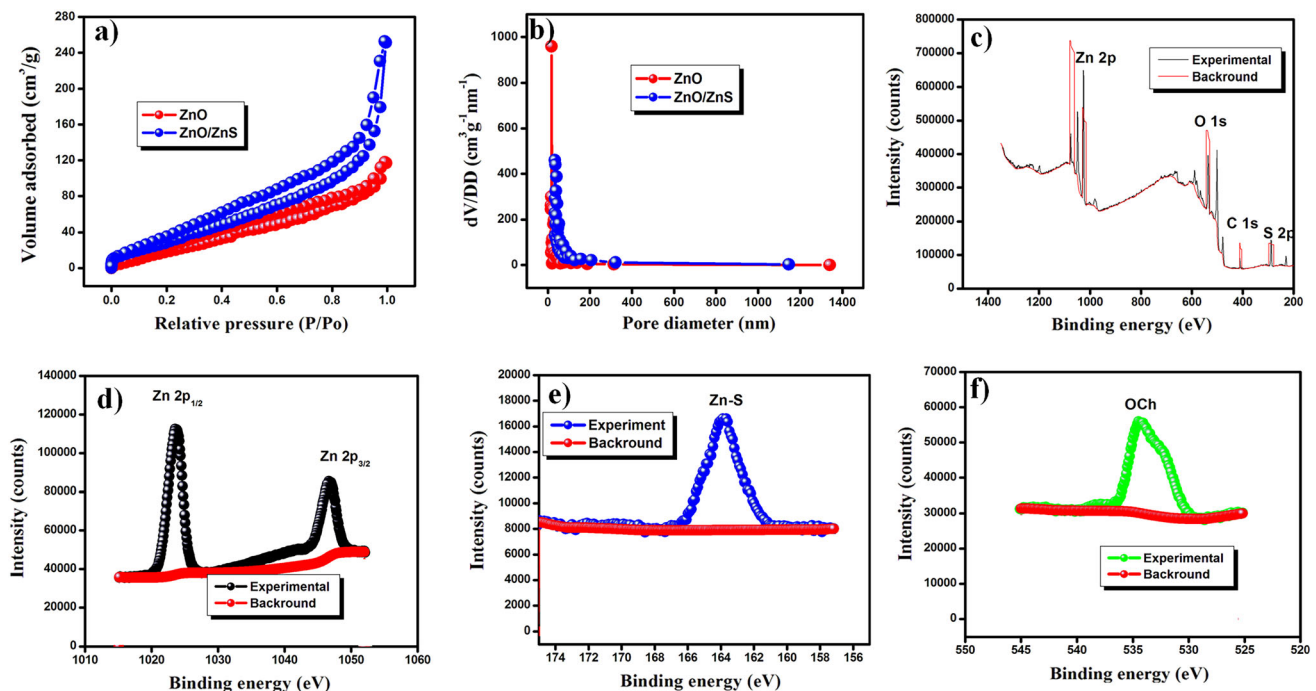


**Fig. 4** a  $\text{N}_2$  adsorption-desorption isotherm; b pore size distribution curves of ZnO and ZnO/ZnS; c XPS survey spectra of ZnO/ZnS; d Ni  $2p$ ; e S  $2p$ ; and f O  $1s$

time was determined. Figure 6a and b shows the temporal degradation profile of MB and RhB under UV light. To keep the catalyst concentration at  $1 \text{ gmL}^{-1}$ , we added ZnS, ZnO, and ZnO/ZnS samples to a 10-M solution of MB and RhB in DI water. After 30 min of supersonic stirring in the dark, there was no significant change in the dye/catalyst solution combination, indicating that equilibrium adsorption had been achieved. For 60 min, both pure ZnO and ZnO/ZnS heterostructures were subjected to the same environment. The concentrations of MB and RhB before and after irradiation are denoted by  $C_0$  and  $C$ , respectively; the deterioration efficiency,  $C/C_0$ , of synthetically produced samples. Degradation of the MB dye molecules has been seen as a general fading of the dyes hue. We observed that after 60 min, 99.5% of the MB dye is destroyed in the ZnO/ZnS heterostructures of sample C, whereas

only 34.5% is degraded in pure ZnO. In a similar way, 28.2% and 87.5% were determined to be the efficiencies of RhB degradation. The photocatalytic activity has been significantly enhanced in ZnO/ZnS heterostructures produced by solution of high sulfur, as shown by the findings. All of the photocatalyst samples are shown in Fig. 6c and d, plotted as  $-\ln C_{\text{dye}}/C_{\text{dye}0}$  of MB and RhB vs. irradiation period. It is evident from the graphs that in both instances the elimination of the dye level follows a linear pattern in this coordinate. Dye removal kinetics of pseudo-first order is shown to be sufficiently fast for both MB and RhB dyes. According to the kinetic data, the ZnO/ZnS photocatalyst degrades MB much more quickly than bare ZnO ( $0.0231 \text{ min}^{-1}$ ). RhB dye rate constants of 0.1139 and  $0.6512 \text{ min}^{-1}$ , respectively, were also determined, demonstrating optimal photocatalytic activity. Table 1 displays the photocatalytic variables.

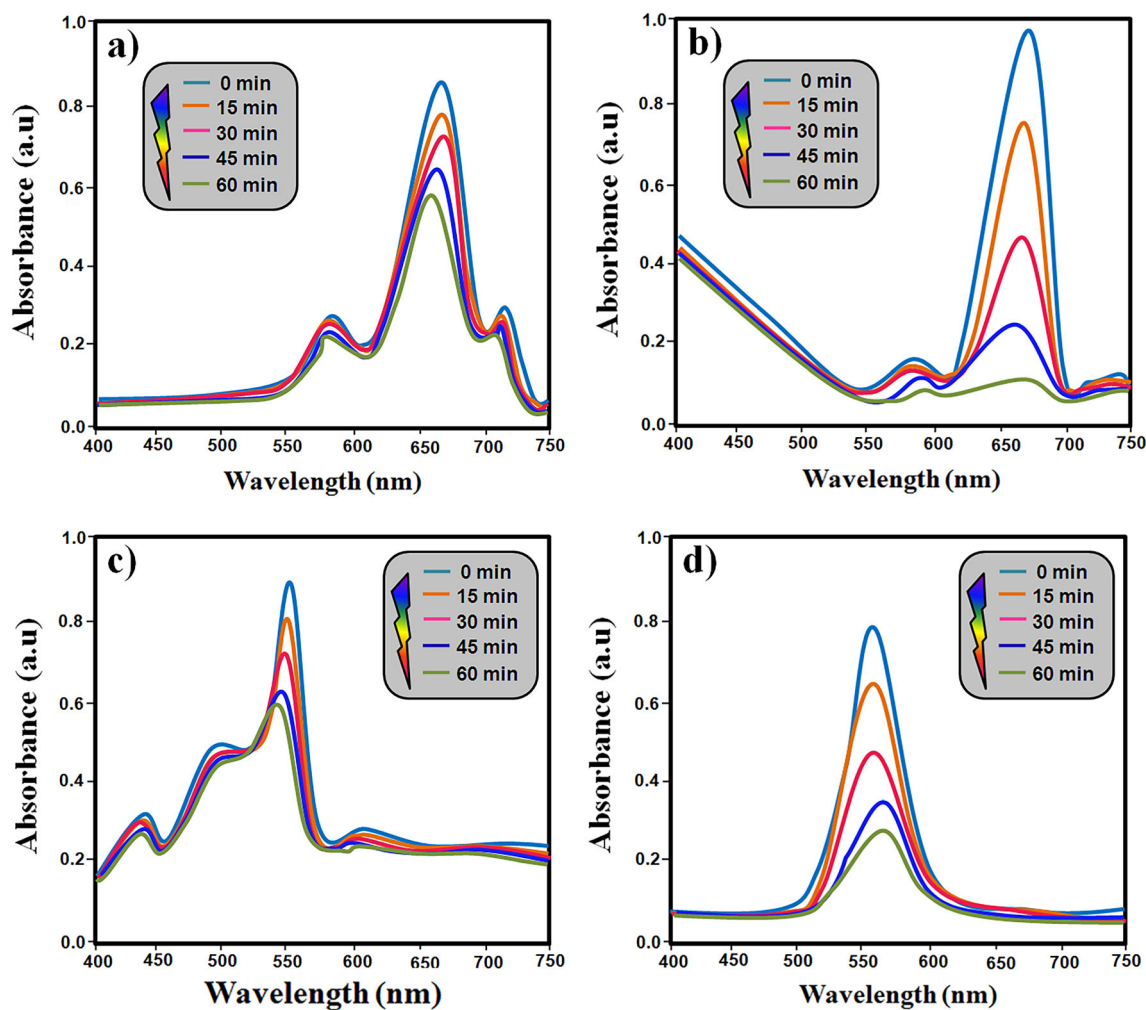


**Fig. 5** UV absorption spectra of MB over **a** ZnO and **b** ZnO/ZnS; UV absorption spectra of RhB over **c** ZnO and **d** ZnO/ZnS



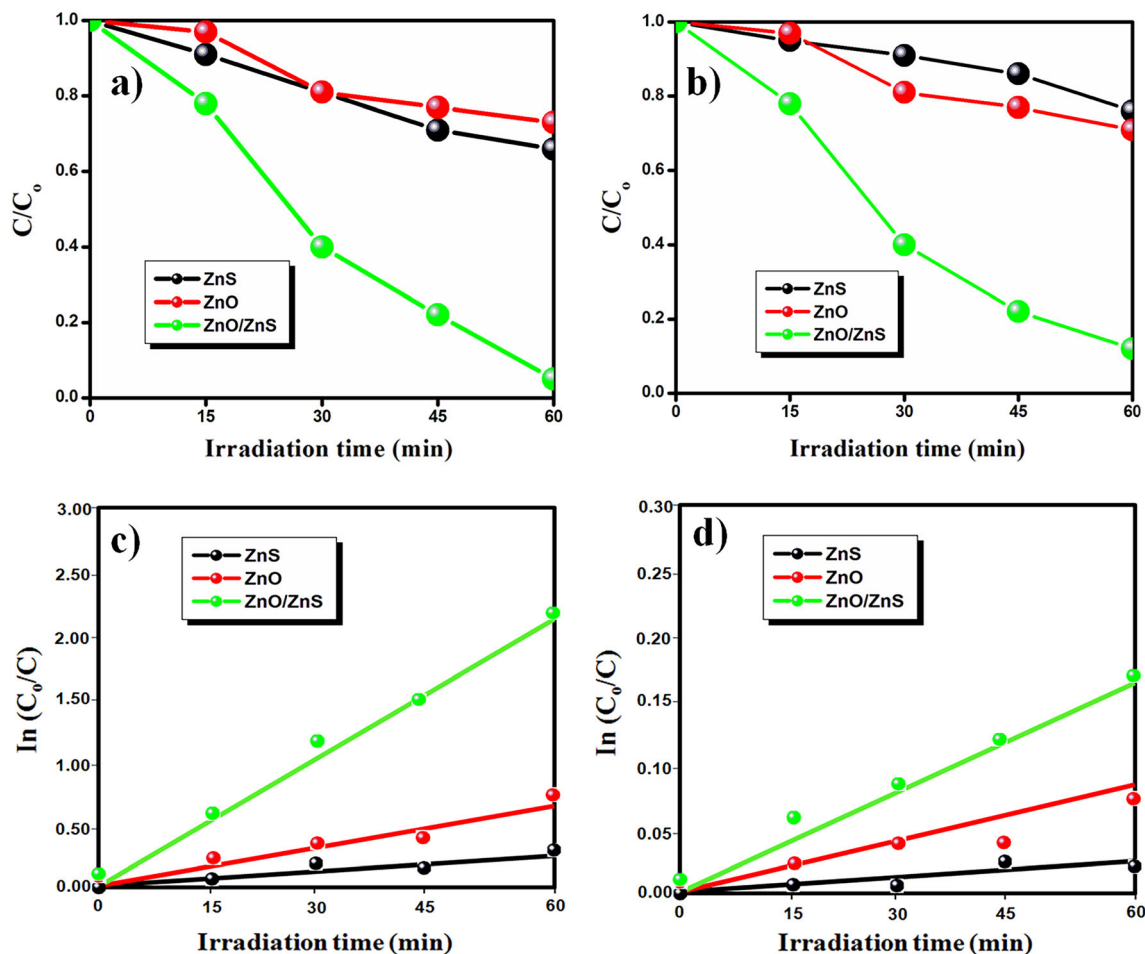


**Fig. 6** a MB degradation efficiency; b RhB degradation efficiency of all the photocatalyst samples under UV light; first-order kinetic plot of c MB; and d RhB using ZnS, ZnO, and ZnO/ZnS photocatalyst samples

Stability and reproducibility are important parameters in the practical device applications of ZnO/ZnS photocatalysts. Therefore, it is necessary to investigate the stability and reusability of the photocatalyst by performing recycling reactions ten times for the photodegradation of MB and RhB solution under UV light irradiation. The 5-mM complex ZnO/ZnS can be used evaluate the reusability of MB solution for ten cycles, as shown in Fig. 7a and b. The dye solutions with the ZnO/ZnS photocatalyst was illuminated under UV light for 3 h, this substrate was rinsed with deionized water to remove the residual MB solution, and dried under a N<sub>2</sub> purge. After ten cycles, the composite photocatalyst maintains the higher reusability of 94.4%. Dye solution pH has a significant impact on degradation rate. Adjusting the solution's pH was shown to hasten the breakdown process, but only up to a point. The pH 7.5 was shown to be the sweet spot for both MB and RhB.

Above this optimal threshold, the rate of photocatalytic degradation slowed down (Fig. 7c and d). The lowest basic pH range was shown to be optimal for MB and RhB breakdown. The effects of MB and RhB dyes at levels ranging from 0.4 to 1.4 × 10<sup>5</sup> M on the rate of photocatalytic degradation were studied. It was shown that a higher concentration of dye resulted in a faster rate of photocatalytic breakdown. This trend may be defined by the fact that a rise in dye concentration made more dye molecules accessible for excitation and energy transmission, leading to a dramatic acceleration in the rate of photocatalytic degradation [30–33]. Under reaction conditions (100 ml of 2 × 10<sup>5</sup> (mol/L), 0.2 g of the sample/100 ml of dye and irradiation time 60 min), holes, hydroxyl radicals, electrons, and superoxide radicals were monitored using KI, isopropanol (IP), silver nitrate (AgN), and benzoquinone (BQ) on pure ZnO and ZnO@ZnS. Figure 8a and b displays the resulting

**Table 1** Photocatalytic activity parameters of ZnS, ZnO, and ZnO/ZnS composite samples

Samples	Rate constant of MB		Rate constant of RhB		MB degradation efficiency (%)	RhB degradation efficiency (%)
	$K$ ( $\text{h}^{-1}$ ) $\text{min}^{-1}$	$R^2$	$K$ ( $\text{h}^{-1}$ ) $\text{min}^{-1}$	$R^2$		
ZnO	0.0031	0.997	0.1139	0.999	34.5	28.2
ZnS	0.0021	0.987	0.1098	0.981	27.8	26.5
ZSM-5/ZnO	0.9541	0.985	0.6512	0.988	99.5	88.5

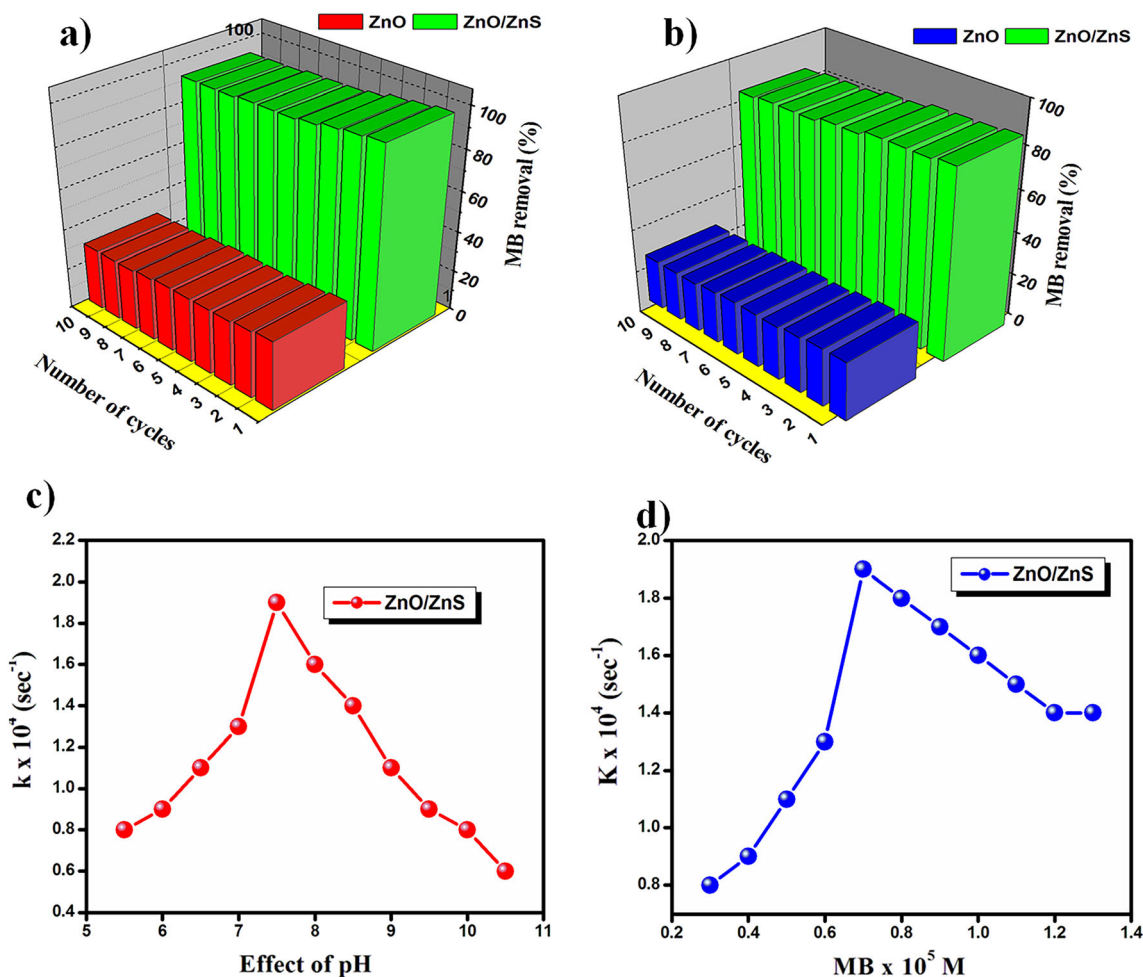


**Fig. 7** The reusability test of the complex ZnO/ZnS core-shell under UV light irradiation. **a** MB and **b** RhB using ZnO/ZnS photocatalyst test under UV light exposure; effect of various

graph. In contrast to other scavengers, the addition of KI considerably increased the photodegradation percentage of MB and RhB. Therefore, the findings indicate that HO radicals could favorably affect the photodegradation of both dyes when exposed to UV radiation. A CHI 660B electrochemical workstation was used to test the samples' photocurrent. Here, we employed a three-electrode set-up consisting of a

reference Ag/AgCl electrode, a counter Pt sheet, and a working FTO glass covered with various samples. It was found, as shown in Fig. 8c, that the photocurrent response signals of ZnO and ZnS were lesser, while the photocurrent signal of ZnO/ZnS photocatalysts were greater during the investigation of the photocatalytic mechanism of ZnO/ZnS. More photogenerated carriers may be formed over the ZnO/ZnS

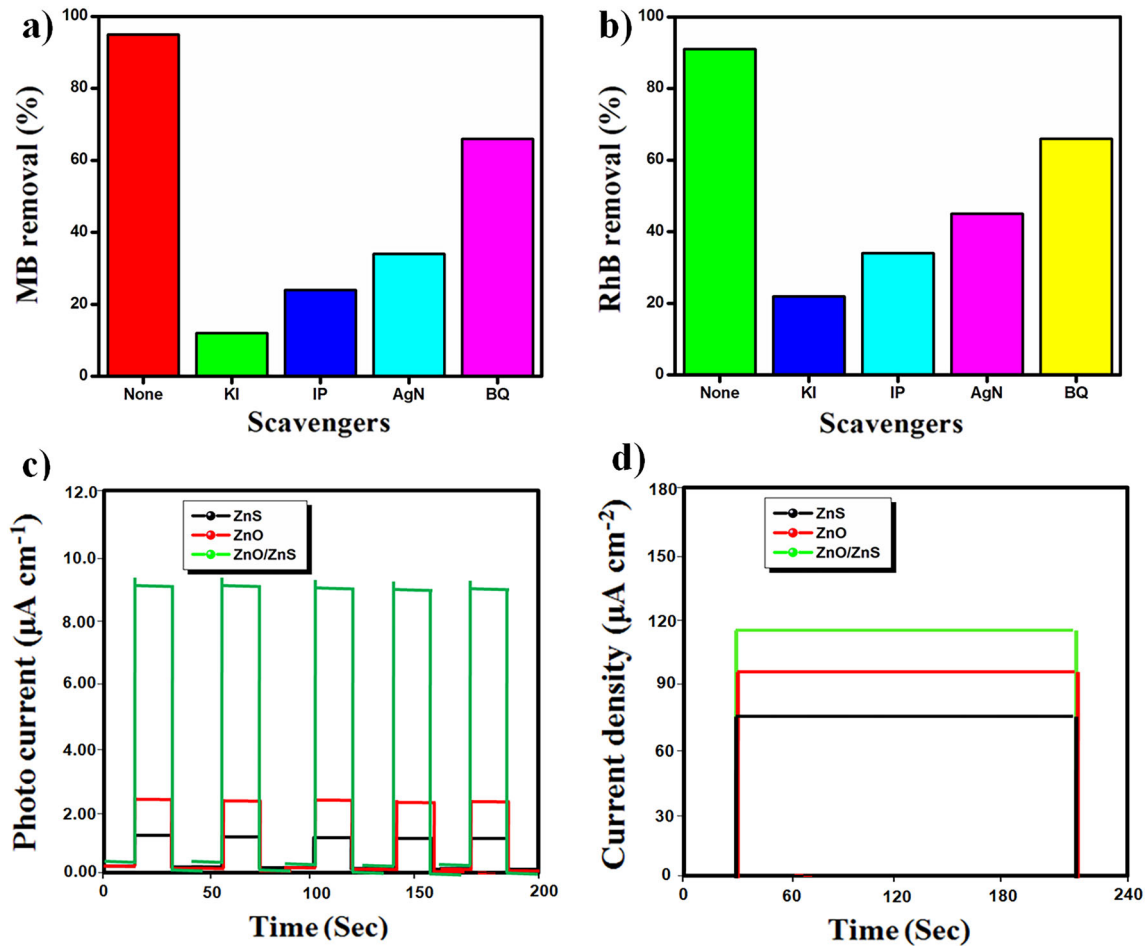


**Fig. 8** Scavenger studies of ZnO/ZnS using **a** MB and **b** RhB under UV light. **c** The photocurrent response curve of ZnO, ZnS, and ZnO/ZnS photocatalyst, respectively, during ten on–off cycles

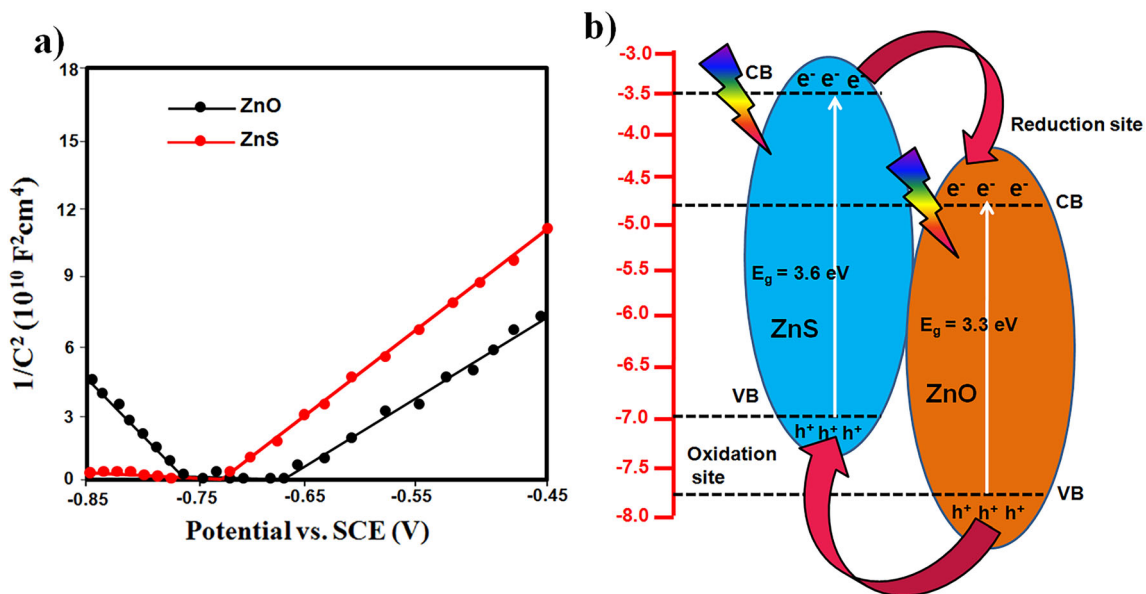
of light irradiation. **d** Time-resolved photocurrent density curves of synthesized samples

photocatalyst under illumination, as shown by the ZnO/ZnS's maximum photocurrent intensity ( $9.3 \text{ A cm}^{-1}$ ) compared to ZnO ( $2.3 \text{ A cm}^{-1}$ ) and ZnS ( $1.2 \text{ A cm}^{-1}$ ) [34]. In addition, as can be seen in Fig. 8d, the photocurrent density did not change much with time for any of the particles up to 325 s, with the greatest values being seen for the ZnO/ZnS photocatalyst particles. The aforesaid photocatalytic findings are consistent with the ZnO/ZnS photocatalyst's ability to efficiently boost the migration rate of carriers and cause it to demonstrate greater photocatalytic activity. As a whole, the data points to a strong photocatalytic efficiency and electrochemical performance for the ZnO/ZnS composite photocatalyst. Table 2 summarizes the findings from this study, which show that the degradation efficiency achieved here is greater than that seen in previously published research [35–40]. From M–S plot in Fig. 9a, it reveals

that both ZnO and ZnS primarily exhibit positive M–S plot slopes, featuring n-type semiconductors. The plots were extrapolated to  $1/C^2 = 0$  to project the value of  $E_{fb}$ , giving  $-0.66 \text{ V}$  and  $-0.62 \text{ V}$  for ZnS and ZnO, respectively. It implies an approximately 40-mV positive shift of flat band potential, which corresponds to a decrease in bending of the band edge, and therefore promotes interfacial charge transfer [41]. It is also observed that ZnO has a gentler slope than that of ZnS, representing higher charge carrier density as compared to bare ZnS. This result is attributed to the additional donor level and higher intrinsic carrier density, which leads ZnO to have improved photo-activated capabilities, thereby absorbing more photon and resulting in higher photogenerated charge carriers. Band structures of the samples provide insight into the process of photocatalysis in ZnO/ZnS heterostructures (Fig. 9b). The

**Table 2** A comparison of photodegradation of MB between the present work and already reported ZnO-based materials

Catalyst	Light source	Experimental conditions for photodegradation	Efficiency (%)	References
ZnO@ZnS dumbbell graphene	Solar simulator (intensity = 80 lux) Philips 18 W/54 1M7	Catalyst: 400 mg/L MB: 3.2 mg/L	94.3	[35]
ZnO@G	Intensity = 14.5 W/m <sup>2</sup> 40 W	Catalyst: 10 mg/L MB: 3.2 mg/L	41.1	[36]
ZnS@ZnO sheets	1.2 mW/cm <sup>2</sup> λ > 400 nm	Catalyst: 500 mg/L MB: 10 mg/L	83.1	[37]
RGO/ZnO@ZIF-8	300W Xe lamp λ > 420 nm	Catalyst: 1 g/L MB: 10 mg/L	82.1	[38]
Cu–ZnO	Sun light	Catalyst: 1 g/L MB: 0.3 mg/L	90.1	[39]
ZnO@ZnS	Sun light	Catalyst: 1 g/L MB: 0.3 mg/L	93.5	[40]
ZnO/ZnS	Intensity = 14.5 W/m <sup>2</sup> 40 W	Catalyst: 10 mg/L MB: 10 mg/L	98.5	This work

**Fig. 9** a Mott–Schottky plots. b Schematics for the electron and hole transfer in the ZnO/ZnS heterostructures under UV light exposure

creation of the ZnS shell has shifted the absorption spectra of the ZnO core to the red. This indicates the production of a type II photocatalytic heterostructure. The resulting band gap is less than that of conventional core–shell composites. Both ZnO and ZnS undergo photoexcitation, a process in which electrons in the valence band (VB) move into the conduction band (CB). Excited electrons go from CB (ZnS) to VB (ZnO), whereas newly formed holes move in the opposite direction, from VB (ZnO) to CB

(ZnS). Recombination of electron–hole pairs in the heterostructure is slowed as a result of this transfer process due to the increased separation between electrons and holes. Photogenerated electrons and holes in the semiconductor react with surface-adsorbed water molecules, releasing reactive oxygen species. Adsorbed oxygen reacts with the free electrons in CB (ZnO) to form the reactive oxygen species,  $\cdot\text{O}_2$ . The adsorbed  $\text{H}_2\text{O}$  molecules react with the holes in VB (ZnS), creating  $\text{OH}\cdot$  species in the



solution. These OH· and ·O<sub>2</sub> species, which are highly oxidative and reductive, respectively, break down the MB molecules into less stable forms, such as water and carbon dioxide. This means the heterostructure is more effective at resisting photodeterioration than either ZnO or ZnS alone.

## 4 Conclusion

In this study, pure ZnO and ZnS nanoparticles as well as ZnO@ZnS core-shell nanocomposites were synthesized by facile hydrothermal method without using any surfactants. Absorbance and PL analysis reveal a remarkable reduction in the band gap energy, limiting the recombination of the charge carriers which in turns leads to increase in the oxidizing power of ZnO/ZnS nanocomposites. The incorporation of ZnO to the surface of ZnS leads to stabilizing zinc oxide particles to decrease the electron-hole pair recombination rate. These results clearly show that the composite ZnO/ZnS showed better activity as compared to individual ZnO and ZnS. The ZnO/ZnS photocatalyst exhibits higher photodegradation (99.5%), high rate constant (0.8761 min<sup>-1</sup>), and desirable stability (loss only 2.9%). ZnO/ZnS photocatalysts were stronger. The ZnO/ZnS showed the highest photocurrent intensity (9.3 μA cm<sup>-1</sup>), which was 4.2 times and 7.5 times than that of ZnO (2.3 μA cm<sup>-1</sup>) and ZnS (1.2 μA cm<sup>-1</sup>), respectively. Photogenerated holes and hydroxyl radicals play a predominant role in dye degradation over ZnO@ZnS nanocomposites. It is expected that the novel photocatalyst which synthesized by simple method and low costs would provide great impetus to the industrialization of photocatalysts.

## Author contributions

AS, SP and RS contributed to study conceptualization and writing (original draft) of the manuscript; SP and CS contributed to data curation, formal analysis, and writing (review and editing) of the manuscript.

## Funding

The authors have not disclosed any funding.

## Data availability

The data that support the findings of this study are available from the corresponding author, upon reasonable request.

## Declarations

**Conflict of interest** The authors declare that there is no conflict of interest regarding the research work reported in this manuscript.

## References

1. H. Ma, X. Cheng, X.D. ChunMa, X. Zhang, M. Xue, X. Zhang, Fu. Yinghuan, Synthesis, characterization, and Photocatalytic activity of N doped ZnO/ZnS composites. *Int J Photoenergy* **2013**, 625024 (2013)
2. S.T. Shishiyanu, T.S. Shishiyanu, O.I. Lupan, Sensing characteristics of tin-doped ZnO thin films as NO<sub>2</sub> gas sensor. *Sens. Actuators B.* **107**, 379–386 (2005)
3. J. Lee, D. Lee, D. Lim, K. Yang, Structural, electrical and optical properties of ZnO: Al films deposited on flexible organic substrates for solar cell applications. *Thin Solid Films* **515**, 6094–6098 (2007)
4. D.H. Zhang, D.E. Brodie, Photoresponse of polycrystalline ZnO films deposited by r.f. bias sputtering. *Thin Solid Films* **261**, 334–339 (1995)
5. J. Luo, S. Zhao, Wu. Panpan, K. Zhang, C. Peng, Sheng Wu Zheng, Synthesis and characterization of new Cd-doped ZnO/ZnS core-shell quantum dots with tunable and highly visible photoluminescence. *J. Mater. Chem. C.* **3**, 3391 (2015)
6. D. Bao, H. Gu, A. Kuang, Sol-gel-derived c-axis oriented ZnO thin films. *Thin Solid Films* **312**, 37–39 (1998)
7. B.Y. Oh, M.C. Geong, T.H. Moon, W. Lee, J.M. Myoung, J.Y. Hwang, D.S. Seo, Transparent conducting ZnO films for liquid crystal displays. *J. Appl. Phys.* **99**, 124505 (2006)
8. U.O. Zgur, Y.I. Alivov, C. Liu, A. Teke, M.A. Reshchikov, S. Dogan, V. Avrutin, S.-J. Cho, H. Morkoc, A comprehensive review of ZnO materials and devices. *J. Appl. Phys.* **98**, 041301 (2005)
9. Y. Feng, W. Hou, X. Zhang, P. Lv, Y. Li, W. Feng, Highly sensitive reversible light-driven switches using electro spun porous aluminum-doped zinc oxide nanofibers. *J. Phys. Chem. C.* **115**, 3956–3961 (2011)
10. W. Park, G. Jo, W.K. Hong, J. Yoon, M. Choe, S. Lee, Y. Ji, G. Kim, Y.H. Kahng, K. Lee, D. Wang, T. Lee, Enhancement in the photodetection of ZnO nanowires by introducing surface-roughness-induced traps. *Nanotechnology* **22**, 205204 (2011)

11. T. Chen, G.Z. Xing, Z. Zhang, H.Y. Chen, T. Wu, Tailoring the photoluminescence of ZnO nanowires using Au nanoparticles. *Nanotechnology* **19**, 435711 (2008)
12. W.I. Park, G.-C. Yi, M.Y. Kim, S.J. Pennycook, Quantum confinement observed in ZnO/ZnMgO nanorod heterostructures. *Adv. Mater.* **15**, 526–529 (2003)
13. S. Biswas, S. Kar, Fabrication of ZnS nanoparticles and nanorods with cubic and hexagonal crystal structures: a simple solvothermal approach. *Nanotechnology* **19**, 045710–045722 (2008)
14. J. Schrier, D.O. Demchenko, L.W. Wang, Optical properties of ZnO/ZnS and ZnO/ ZnTe heterostructures for photovoltaic applications. *Nano Lett.* **7**, 2377–2382 (2007)
15. A. Bera, D. Basak, Photoluminescence and photoconductivity of ZnS-coated ZnO nanowires. *Appl. Mater. Interface* **2**, 408–412 (2010)
16. J. Yan, X.S. Fang, L.D. Zhang, Y. Bando, U.K. Gautam, B. Dierre et al., Structure and cathodoluminescence of individual ZnS/ZnO biaxial nanobelt heterostructures. *Nano Lett.* **8**, 2794–2799 (2008)
17. G.Z. Shen, D. Chen, C.J. Lee, Hierarchical saw-like ZnO nanobelt/ZnS nanowire heterostructures induced by polar surfaces. *J. Chem. Phys. B* **110**, 15689–15693 (2006)
18. C.-C. Cheng, W.C. Weng, H.I. Lin, J.L. Chiu, Yu. Hong-Yu Jhao, T.A. Liao, Y. Chang Tze Ricky, H. Chen, *RSC Adv* **8**, 26341–26348 (2018)
19. T. Ghrib, M.A. Al-Messiere, A.L. Al-Otaibi, Synthesis and characterization of ZnO/ZnS core/shell nanowires. *J. Nanomater.* (2014). <https://doi.org/10.1155/2014/989632>
20. A.D. Dinsmore, D.S. Hsu, H.F. Gray, S.B. Qadri, Y. Tian, B.R. Ratna, Mn-doped ZnS nanoparticles as efficient low-voltage cathodoluminescent phosphors. *Appl. Phys. Lett.* **75**, 802–804 (1999)
21. R. Maity, K.K. Chattopadhyay, Synthesis and optical characterization of ZnS and ZnS: Mn nanocrystalline thin films by chemical route. *Nanotechnology* **15**, 812–816 (2004)
22. S. Mahamuni, K. Borgohain, B.S. Bendre, V.J. Leppert, S.H. Risbud, Spectroscopic and structural characterization of electrochemically grown ZnO quantum dots. *J. Appl. Phys.* **85**, 2861–2865 (1999)
23. A.E. Shalan, A.M. Elseman, M. Rasly, M.M. Moharam, M.L. Cantu, M.M. Rashad, Concordantly fabricated heterojunction ZnO–TiO<sub>2</sub> nanocomposite electrodes via a co-precipitation method for efficient stable quasi-solid-state dye-sensitized solar cells. *RSC Adv.* **5**, 103095–103104 (2015)
24. S.-H. Wu, D.-H. Chen, Synthesis of high-concentration Cu nanoparticles in aqueous CTAB solutions. *J. Colloid Interface Sci.* **273**, 165–169 (2004)
25. M. Parthibavarman, M. Karthik, P. Sathishkumar, R. Poon-guzhali, Rapid synthesis of novel Cr-doped WO<sub>3</sub> nanorods: an efficient electrochemical and photocatalytic performance. *J. Iran. Chem. Soc.* **15**, 1419–1430 (2018)
26. R. BoopathiRaja, M. Parthibavarman, Hetero-structure arrays of MnCo<sub>2</sub>O<sub>4</sub> nanoflakes@ nanowires grown on Ni foam: Design, fabrication and applications in electrochemical energy storage. *J. Alloy. Compd.* **811**, 152084 (2019)
27. R. BoopathiRaja, M. Parthibavarman, A. Nishara Begum, Hydrothermal induced novel CuCo<sub>2</sub>O<sub>4</sub> electrode for high performance supercapacitor applications. *Vacuum* **165**, 96–104 (2019)
28. X.-X. Gao, J. Wang, J.-L. Yu, H.-B. Xu, Novel ZnO-ZnS nanowire arrays with heterostructures and enhanced photocatalytic properties. *Cryst. Eng. Comm.* **17**, 6328–6337 (2015)
29. G.-H. Yue, P.-X. Yan, D. Yan, X.-Y. Fan, M.-X. Wang, D.-M. Qu, J.Z. Liu, Hydrothermal synthesis of single-crystal ZnS nanowires. *Appl. Phys. A* **84**, 409–412 (2006)
30. N. Sharma, R. Jha, S. Baghel, D. Sharma, Study on photocatalyst zinc oxide annealed at different temperatures for photodegradation of Eosin Y dye. *J. Alloy. Compd.* **695**, 270–279 (2017)
31. L. Yang, X. Wang, F. Yang, X. Yang, Excellent antimicrobial properties of mesoporous anatase TiO<sub>2</sub> and Ag/TiO<sub>2</sub> composite films. *Microporous Mesoporous Mater.* **114**, 431–439 (2008)
32. C. Oana, C.L. Huisman, A. Reller, Photoinduced reactivity of titanium dioxide. *Prog. Solid State Chem.* **32**, 33–177 (2004)
33. P.G. Li, A. Bono, D. Krishnaiah, J.G. Collin, Preparation of titanium dioxide photocatalyst loaded onto activated carbon support using chemical vapor deposition: a review paper. *J. Hazard. Mater.* **157**, 209–219 (2008)
34. F. Zhang, Y.C. Zhang, Y.Y. Wang, A.P. Zhu, Y. Zhang, Efficient photocatalytic reduction of aqueous Cr (VI) by Zr<sup>4+</sup> doped and polyaniline coupled SnS<sub>2</sub> nanoflakes. *Sep. Purif. Technol.* **283**, 120161 (2022)
35. X. Yu, G. Zhang, H. Cao, ZnO@ZnS hollow dumbbells graphene composites as high-performance photocatalysts and alcohol sensors. *New J. Chem.* **36**, 2593–2598 (2012)
36. B.M. Rajbongshi, A. Ramchiary, S.K. Samdarshi, Influence of N-doping on photocatalytic activity of ZnO nanoparticles under visible light irradiation. *Mater. Lett.* **134**, 111–114 (2014)
37. X. Yu, P. Wei, Y. Li, Enhanced sunlight photocatalytic performance of ZnO/ZnS binary heterostructure sheets. *Mater. Lett.* **240**, 284–286 (2019)
38. G. Zhu, X. Li, H. Wang, L. Zhang, Microwave assisted synthesis of reduced graphene oxide incorporated MOF-derived ZnO composites for photocatalytic application. *Catal. Commun.* **88**, 5–8 (2017)

39. S. Kuriakose, B. Satpati, S. Mohapatra, Highly efficient photocatalytic degradation of organic dyes by Cu doped ZnO nanostructures. *Phys. Chem. Chem. Phys.* **17**, 25172–25181 (2015)
40. M.F. Sanad, A.E. Shalan, S.M. Bazid, S.M. Abdelbasir, Pollutant degradation of different organic dyes using the photocatalytic activity of ZnO@ZnS nanocomposite. *J. Environ. Chem. Eng.* **6**, 3981–3990 (2018)
41. M. Ye, J. Gong, Y. Lai, C. Lin, Z. Lin, High-efficiency photoelectrocatalytic hydrogen generation enabled by palladium quantum dots-sensitized TiO<sub>2</sub> nanotube arrays. *J. Am. Chem. Soc.* **134**, 15720–15723 (2012)

**Publisher's Note** Springer Nature remains neutral with regard to jurisdictional claims in published maps and institutional affiliations.

Springer Nature or its licensor (e.g. a society or other partner) holds exclusive rights to this article under a publishing agreement with the author(s) or other rightsholder(s); author self-archiving of the accepted manuscript version of this article is solely governed by the terms of such publishing agreement and applicable law.